Check for updates

Geophysical Research Letters

RESEARCH LETTER
10.1029/2026GL122790

From Shadow to Fertilizer: Slanted Sunlight in 3D Radiation Enhances Cloud Condensate, Size, and Lifetime of Shallow Cumulus

Xiaocong Wang[1] and **Yanjie Liu**[1,2]

[1]Institute of Atmospheric Physics (IAP), Chinese Academy of Sciences (CAS), Beijing, China, [2]College of Earth and Planetary Sciences, University of Chinese Academy of Sciences (UCAS), Beijing, China

Key Points:

- 3D radiation produces higher cloud tops and greater cloud condensate than 1D radiation
- 3D radiation favors the development of larger and longer-lived clouds, at the expense of smaller and short-lived clouds
- Land-air coupling enhances the development of larger and long-lived clouds under 3D radiation but tends to suppress it under 1D radiation

Supporting Information:

Supporting Information may be found in the online version of this article.

Correspondence to:

X. Wang,
wangxc@lasg.iap.ac.cn

Citation:

Wang, X., & Liu, Y. (2026). From shadow to fertilizer: Slanted sunlight in 3D radiation enhances cloud condensate, size, and lifetime of shallow cumulus. *Geophysical Research Letters*, *53*, e2026GL122790. https://doi.org/10.1029/2026GL122790

Received 8 MAR 2026
Accepted 2 JUL 2026

© 2026 The Author(s). Geophysical Research Letters published by Wiley Periodicals LLC on behalf of American Geophysical Union.
This is an open access article under the terms of the Creative Commons Attribution License, which permits use, distribution and reproduction in any medium, provided the original work is properly cited.

Abstract The impact of three-dimensional (3D) shortwave radiation on cloud condensate, size and lifetime is investigated using large-eddy simulations coupled to an interactive land surface model (LSM). Results show 3D radiation produces higher cloud tops and greater cloud condensate than 1D radiation, resulting from larger downward shortwave fluxes beneath clouds. The enhanced radiative flux leads to increased surface temperature, which in turn amplifies sensible and latent heat fluxes beneath clouds by about 40%, thereby promoting further cloud development. 3D radiation produces larger and longer-lived clouds than 1D radiation, with the tail in size distribution occurring near 1,400 m in 3D-LSM versus 1,100 m in 1D-LSM. These differences arise from the contrasting surface heterogeneity induced by the 1D and 3D radiation schemes. Unlike 1D-LSM, where cloud shadows fall directly beneath clouds and locally suppress updrafts, 3D-LSM displaces shadows, favoring cloud-scale circulations that provide positive feedback, leading to thicker, larger, and longer-lived clouds.

Plain Language Summary Clouds play an important role in regulating Earth's energy and water cycles, yet their representation in models depends strongly on how radiation and land–atmosphere interactions are treated. Many models still use simplified one-dimensional (1D) radiation schemes that neglect the three-dimensional (3D) effects of cloud scattering. Using large-eddy simulations coupled with an interactive land surface model (LSM), we show that accounting for 3D shortwave radiation substantially alters cloud evolution. Compared to 1D radiation, 3D radiation allows more sunlight to reach the surface beneath clouds, primarily because its direct component remains nearly unchanged with increasing cloud thickness, in stark contrast to the sharp decline observed in 1D radiation. This additional energy increases surface heat and moisture fluxes, which in turn promotes deeper, larger, and longer-lived clouds. Our results further indicate that in 1D-LSM, cloud shadows fall directly beneath clouds, suppressing local updrafts. This negative feedback keeps clouds even smaller and shorter-lived than in the simulation without land-surface coupling. These findings highlight the importance of representing 3D radiative effects for realistic simulations of cloud properties and their interaction with the land surface.

1. Introduction

Clouds, especially shallow cumulus, are a major source of uncertainty in climate feedback and sensitivity (Bony & Dufresne, 2005; Sherwood et al., 2020; Su et al., 2014; Wang et al., 2008; Zelinka et al., 2020). Although large horizontal variability in their microphysical properties has been observed and simulated (Lu et al., 2012; Wang & Zhang, 2014; Zhang et al., 2017; Zhao et al., 2024), progress in parameterizing their radiative effects remains limited. Virtually all radiative transfer schemes account for cloud inhomogeneity via independent column approximations that neglect horizontal photon transport (Räisänen et al., 2004; Wang, 2017; Wang et al., 2021), or through simplified two-stream methods (Barker et al., 2015; Hogan et al., 2016; Meador & Weaver, 1980; Yang et al., 2019). Radiative transfer, however, is inherently three-dimensional (3D hereafter), involving photon transport in both the horizontal and vertical directions (Mayer, 2009). While ignoring horizontal exchange is acceptable at coarse resolution, it introduces substantial errors in high-resolution simulations (Cahalan et al., 1994). In these high-resolution models, the horizontal scale of clouds and grid cells is typically smaller than the vertical depth. Consequently, cloud shadows can reside in different grid cells than the clouds under 3D radiation, whereas 1D radiation always places shadows directly underneath the clouds. This leads to differences in surface solar radiation and subsequent cloud development via surface heat flux heterogeneity. Offline studies have demonstrated that 3D radiative effects are crucial for accurately capturing the spatial distribution of surface

19448007, 2026, 14, Downloaded from https://agupubs.onlinelibrary.wiley.com/doi/10.1029/2026GL122790, Wiley Online Library on [17/07/2026]. See the Terms and Conditions (https://onlinelibrary.wiley.com/terms-and-conditions) on Wiley Online Library for rules of use; OA articles are governed by the applicable Creative Commons License

shortwave radiation (e.g., Gristey et al., 2020; Tijhuis et al., 2023, 2024). Similar effects on surface radiation can also arise from mountainous terrain (Gu et al., 2012).

To fully capture the impact of 3D radiation on cloud development, coupling an accurate 3D radiative transfer scheme with both the flow solver and a land surface model is necessary. Due to high computational cost, most studies have used simplified approaches. Using the Tilted Independent Column Approximation (TICA), Wapler and Mayer (2008) found that under a zero-zenith angle, cloud lifetime was reduced, while cloud cover and liquid water path remained largely unchanged. Gronemeier et al. (2017) showed that displaced cloud shadows can generate secondary circulations and extend cloud lifetime at large zenith angles. Using a more accurate 3D solver (Jakub & Mayer, 2015), Jakub and Mayer (2017) demonstrated that coupled 3D radiation promotes cloud streets via surface heat flux heterogeneity. Veerman et al. (2020) showed that coupled 3D radiation yields larger and thicker clouds. While most existing studies are essentially sensitivity analyses that examine factors such as solar zenith angle, azimuth angles, and background wind, few have quantitatively examined the influence of 3D radiation on cloud evolution using a realistic field case. To address this gap, we employ a LES model coupled with a 3D radiative transfer scheme, applied to a shallow cumulus case from a field campaign. We quantify the impact of 3D versus 1D radiation on cloud condensate, size, and lifetime, and also compare simulations with and without land-atmosphere coupling to isolate the role of surface-atmosphere feedback.

2. Model, Methods, and Case Description

2.1. LES Model

We used the parallelized LES model (PALM), version 6.0 (Maronga et al., 2020), which has been widely applied to studies of convective boundary layers (e.g., Maronga & Raasch, 2013; Raasch & Franke, 2011). PALM solves the non-hydrostatic incompressible Navier–Stokes equations under either the Boussinesq or anelastic approximation. The model adopts a fifth-order advection scheme (Wicker & Skamarock, 2002) and a third-order Runge-Kutta time-stepping scheme (Williamson, 1980). For cloud process, an all-or-nothing saturation adjustment scheme is employed according to Cuijpers and Duynkerke (1993), which assumes no subgrid-scale fluctuations within a host grid. The calculation of cloud droplet effective radius is based on the diagnosed liquid water content and a prescribed constant droplet number concentration following Martin et al. (1994). Subgrid-scale turbulence is parameterized using a 1.5-order closure (Deardorff, 1980), implemented in the form described by Saiki et al. (2000). The land-surface model (LSM) in PALM is based on the Tiled ECMWF Scheme for Surface Exchanges over Land, which solves the surface energy balance using a resistance-based parameterization for turbulent fluxes (Balsamo et al., 2009). To incorporate 3D radiative effects, PALM is coupled with the TenStream radiative transfer scheme (Jakub & Mayer, 2015), an efficient parallel solver for the full 3D radiative transfer equation that explicitly computes radiative exchange coefficients for sideward energy streams.

2.2. Case Description

The shallow convection case is based on observations from the Atmospheric Radiation Measurement (ARM) Southern Great Plains (SGP) central facility on 21 June 1997, during which shallow cumuli developed over a dry land surface (Brown et al., 2002). The PALM model uses a horizontal domain of 128 × 128 grid points with a spacing of 100 m. Vertically, the model extends from the surface to 4,000 m with a uniform resolution of 40 m. The initial sounding is taken from Brown et al. (2002), while the large-scale forcing to drive the model is derived using a variational analysis method (Zhang & Lin, 1997). Three experiments were conducted: (a) 3D-LSM: a simulation with TenStream radiative transfer and interactive land-surface coupling; (b) 1D-LSM: a simulation with two-stream radiative transfer and interactive land-surface coupling; (c) No-LSM: a simulation without land-surface coupling, in which surface heat fluxes are prescribed from the domain-averaged, time-varying fluxes of 1D-LSM. This configuration is equivalent to horizontally homogenizing the surface fluxes in 1D-LSM. To isolate the impact of cloud-shadow-induced surface heterogeneity on cloud evolution, longwave radiation is turned off, and radiative heating is not interactively fed back to the flow solver in the two radiation-enabled experiments. Besides, a motionless background state is adopted, a configuration in favor of amplifying the impact of 3D radiation on cloud development (Gronemeier et al., 2017). Each simulation is integrated for 14 hr, with full 3D model output saved at 1-min intervals. In terms of computational cost, the 3D radiation scheme is roughly 17 times more expensive than its 1D counterpart in our setup.

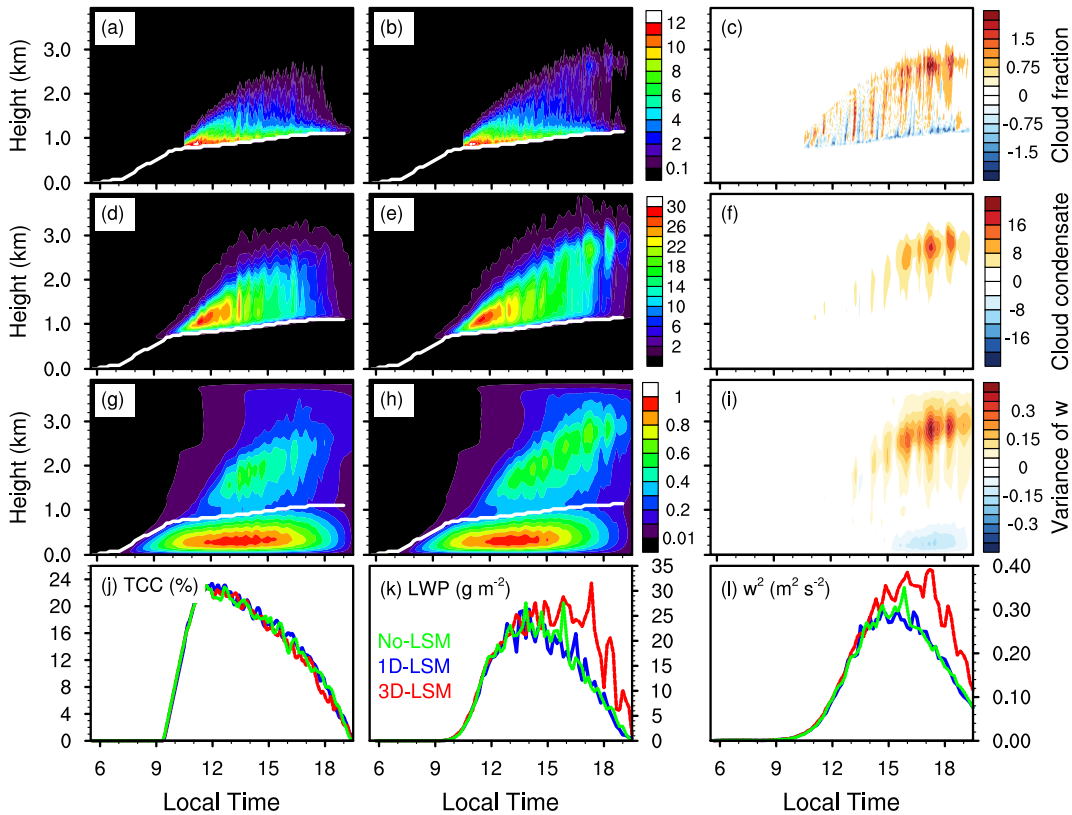


Figure 1. Time-height cross-sections of domain-averaged cloud fraction (a–c), cloud condensate (d–f), and vertical velocity variance (g–i) for the experiments of 1D-LSM (left column), 3D-LSM (middle column), and their differences (right column). White lines denote the boundary layer top. Time series of total cloud cover (j), liquid water path (k), and vertically averaged vertical velocity variance (l) are shown in the lower panels. Units are % for cloud fraction, mg kg^{-1} for cloud condensate, and m^2 s^{-2} for velocity variance.

2.3. Cloud-Tracking Procedure

To examine the impact of 3D versus 1D radiation on cloud statistics, cloud tracking was conducted during post-processing using the algorithm detailed in Dawe and Austin (2012). Three regions are defined for cloud tracking: (a) cloud "core," defined as model points containing liquid water and having positive buoyancy and upward velocity; (b) "condensed," defined as all grid points containing liquid water; (c) "plume," the region of upward-moving air that is associated with the cloud. The primary tracked region is the "condensed" region, whereas the "core" and "plume" regions serve auxiliary roles: they help determine when two clouds should be considered merged (via core connectivity) and when a split is genuine (via plume connectivity to the surface). After tracking, each time step yields a list of grid boxes associated with clouds and plumes. This output enables the determination of cloud size, and the number of clouds present at any given time. Cloud lifetime is then calculated as the length of time that a cloud is tracked.

3. Results and Analysis

3.1. Shallow Cumulus Evolution

The first two rows of Figure 1 present the time-height cross-sections of domain-averaged cloud fraction and cloud condensate for the 1D-LSM and 3D-LSM experiments. The results for the No-LSM experiment closely resemble those of 1D-LSM (Figure S1 in Supporting Information S1). After approximately 9:00 LST (local solar time), all simulations start to produce condensate above the convective boundary layer (CBL) top (white curve), defined as the height where the buoyancy flux has a local minimum following Khairoutdinov and Randall (2006). Prior to this, the variance of vertical velocity above the CBL remains relatively low (Figures 1g and 1h). Thereafter, both the variance of vertical velocity and cloud condensate increase gradually, remain relatively steady, and then

19448007, 2026, 14, Downloaded from https://agupubs.onlinelibrary.wiley.com/doi/10.1029/2026GL122790, Wiley Online Library on [17/07/2026]. See the Terms and Conditions (https://onlinelibrary.wiley.com/terms-and-conditions) on Wiley Online Library for rules of use; OA articles are governed by the applicable Creative Commons License

19448007, 2026, 14, Downloaded from https://agupubs.onlinelibrary.wiley.com/doi/10.1029/2026GL122790, Wiley Online Library on [17/07/2026]. See the Terms and Conditions (https://onlinelibrary.wiley.com/terms-and-conditions) on Wiley Online Library for rules of use; OA articles are governed by the applicable Creative Commons License

decline sharply during the decaying phase. The CBL height near the end of simulation (17:00 LST) reaches as high as 1.1 km, which is in good agreement with Guo et al. (2021). While all experiments reproduce such characteristic evolution of continental shallow convection, their detailed structures differ. Relative to 1D-LSM, 3D-LSM produces higher cloud tops (Figure 1c), greater cloud condensate (Figure 1f), and enhanced vertical velocity variance (Figure 1i). These contrasts are more pronounced in integrated quantities: liquid water path (LWP), and vertically averaged vertical velocity variance. Notably, LWP in 3D-LSM rises to over 30 g m^{-2} by 17:00 LST, while it peaks at about 25 g m^{-2} (14:00 LST) in 1D-LSM and around 27 g m^{-2} (16:00 LST) in No-LSM (Figure 1k). The higher LWP in 3D-LSM is primarily due to increased cloud thickness (Figure S2 in Supporting Information S1). Correspondingly, the vertically averaged vertical velocity variance reaches about 0.4 m^2 s^{-2} in 3D-LSM, compared to 0.28 m^2 s^{-2} in 1D-LSM and 0.34 m^2 s^{-2} in No-LSM experiments (Figure 1l). These results align broadly with the findings of Veerman et al. (2020), who also reported that coupled 3D radiation yields thicker clouds, even though different LES models and case setups were employed. 3D-LSM produces increased layer cloud fraction at middle and upper levels and decreased cloud fraction at lower levels (Figure 1c), but the total cloud cover remains comparable across all three experiments (Figure 1j). This outcome is attributable to partial compensation between the increase in cloud fraction at middle and upper levels and the decrease at lower levels. Most striking is that total cloud cover peaks earlier (11:30 LST) than LWP and declines afterward, despite the continued vertical growth of clouds. This arises because the layer cloud fraction near cumulus base peaks during the initial stage (Figures 1a and 1b), due to the initially disorganized nature of cumulus parcels and frequent detrainment that spreads condensate within this layer.

To elucidate the mechanisms underlying the differences between 3D-LSM and 1D-LSM experiments, Figure 2 presents the domain-averaged and cloud-averaged (i.e., averaged only over cloudy columns) downward shortwave radiative flux, its direct and diffuse components, surface temperature, sensible heat flux, and latent heat flux from the two simulations. As noticed, domain-averaged surface fluxes and surface temperature remain similar throughout the integration period, which arises because, on a domain-mean basis, increases or decreases in the direct and diffuse radiation components compensate each other (Figures 2b and 2c). Beneath clouds, however, both surface fluxes and temperature differ markedly between the two simulations. After cloud formation at 9:00 LST, the downward shortwave flux is substantially larger in 3D-LSM than in 1D-LSM, leading to higher surface temperature, sensible heat flux, and latent heat flux. These differences generally intensify with increasing solar zenith angle, leading to greater contrasts during sunrise and sunset, whereas they remain relatively small between 12:00 and 13:00 LST. On average over the period, the differences between the two experiments reach approximately 216 W m^{-2} in downward shortwave radiation, 20 W m^{-2} in sensible heat flux, and 104 W m^{-2} in latent heat flux, corresponding to roughly 40% of the respective values in 1D-LSM. The decomposition of total radiation reveals that the direct component in 3D-LSM is substantially larger than in 1D-LSM by approximately 288 W m^{-2}, while the diffuse component is only slightly reduced by about 72 W m^{-2}. These results show that 3D-LSM enhances surface fluxes beneath clouds, whereas they are typically reduced in 1D-LSM. This implies contrasting spatial heterogeneity in surface fluxes between the two experiments, with the pattern in 1D-LSM primarily driven by traditional cloud radiative effects.

In order to understand why 3D-LSM yields larger downward shortwave flux than 1D-LSM, we decompose the total downward shortwave flux into its direct and diffusion components. Because thicker clouds scatter and absorb more incident solar radiation, the total downward shortwave radiation and the partition between direct and diffuse components depend on cloud thickness. We therefore examine the response of surface heat fluxes to cloud thickness using LWP as a proxy. Local values of the direct and diffuse components of downward shortwave flux, surface temperature, sensible heat flux, and latent heat flux are binned by LWP. The resulting binned values are then averaged over the model output between 13:00 and 14:00 LST, as shown in Figure 3. In 1D-LSM, downward shortwave flux decreases monotonically with increasing LWP (Figure 3a), primarily due to a reduction in the direct component. For clouds with LWP below about 50 g m^{-2} (corresponding to an optical depth of ~7.5), the diffuse component increases with LWP, a consequence of enhanced conversion of direct to diffuse radiation through cloud scattering. Beyond an LWP of 50 g m^{-2}, the diffuse component also decreases with increasing LWP, albeit more gradually than the direct component. In 3D-LSM, the direct component remains nearly invariant with LWP, whereas the diffuse component increases throughout the entire LWP range. This arises because some of the direct light reaching a point may come from different columns through side illumination. As a result, when we bin surface points by the LWP of the column directly above them, the average direct flux shows a weak dependence on that local LWP. For diffuse radiation, a surface point beneath a thick cloud can receive

19448007, 2026, 14, Downloaded from https://agupubs.onlinelibrary.wiley.com/doi/10.1029/2026GL122790, Wiley Online Library on [17/07/2026]. See the Terms and Conditions (https://onlinelibrary.wiley.com/terms-and-conditions) on Wiley Online Library for rules of use; OA articles are governed by the applicable Creative Commons License

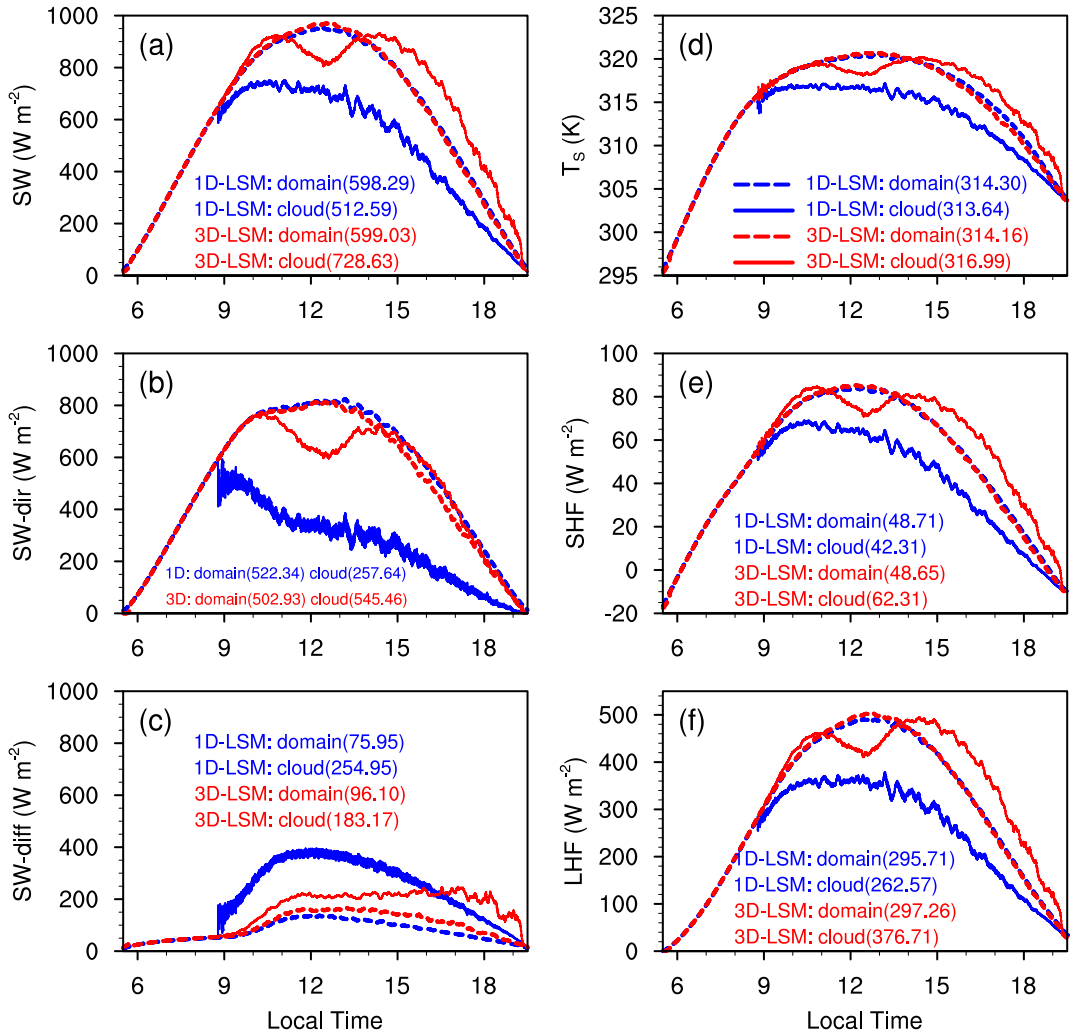


Figure 2. Time series of domain-averaged (dashed lines) and cloud-averaged (solid lines) downward shortwave radiation (a), its direct (b) and diffuse (c) components, surface temperature (d), sensible heat flux (e), and latent heat flux (f). Blue curves denote the 1D-LSM experiment and red curves the 3D-LSM experiment. The numbers in each panel indicate the time-averaged values.

diffuse radiation from adjacent thinner clouds or clear gaps via horizontal transport. Therefore, the bin-averaged diffuse flux for high-LWP points becomes enhanced because they receive scattered light from their less-attenuating surroundings while also benefiting from the strong scattering capacity of the thick cloud itself. Consequently, total downward shortwave flux increases with LWP in 3D-LSM but decreases in 1D-LSM. In turn, surface heat fluxes and surface temperature in 3D-LSM rise moderately with LWP, in line with the enhanced downward radiative energy reaching the surface. This creates a favorable environment for preexisting clouds by boosting the supply of enthalpy fluxes from the surface, thereby promoting further cloud development (Chen et al., 2020; Ren et al., 2023).

3.2. Cloud Size and Lifetime

In this subsection, we examine the feedback of cloud-shadow-induced surface heterogeneity on cloud size statistics using the cloud-tracking procedure described in Section 2.3. Following Neggers et al. (2003), cloud size is defined as the square root of a cloud's horizontal area. Data points are collected in bins of 30-m width at 1-min intervals over the entire simulation period. The cloud-size distribution at each height for the 1D-LSM experiment is shown in Figure 4a. The distribution peaks at small cloud sizes and decreases toward larger sizes. The results for the No-LSM experiment closely resemble those of 1D-LSM (Figure S3 in Supporting Information S1). Compared

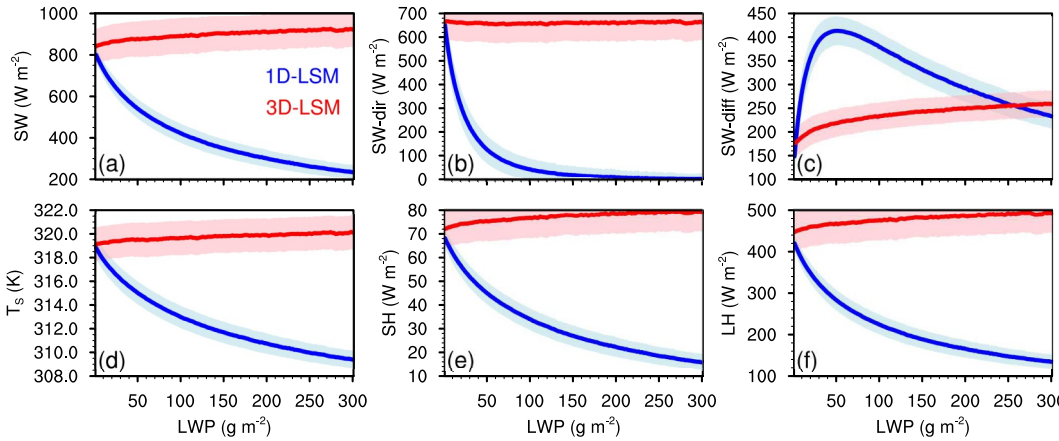


Figure 3. Mean downward shortwave flux (a), its direct (b) and diffuse (c) components, surface temperature (d), sensible heat flux (e), and latent heat flux (f) as a function of liquid water path bin, averaged between 14:00 and 15:00 LST. Blue curves denote the 1D-LSM experiment and red curves the 3D-LSM experiment. The shading indicates the width of twice the standard deviation of the results between 14:00 and 15:00 LST.

with 1D-LSM, 3D-LSM exhibits not only higher cloud tops but also more large clouds at the expense of fewer small clouds (Figure 4b), a contrast that is more evident in their difference (Figure 4c). We also project the clouds' condensed regions onto a horizontal plane to simulate what a satellite directly overhead would observe; the resulting size distribution is shown in Figure 4d. While Figure 4d shows frequency, the cloud number statistics exhibit a similar distribution (Figure S4a in Supporting Information S1). Despite the close resemblance between 1D-LSM and No-LSM for clouds smaller than 1,000 m, 1D-LSM produces fewer larger clouds (size >1,000 m) than No-LSM. The size distribution generally follows a power-law decay toward larger clouds, with the

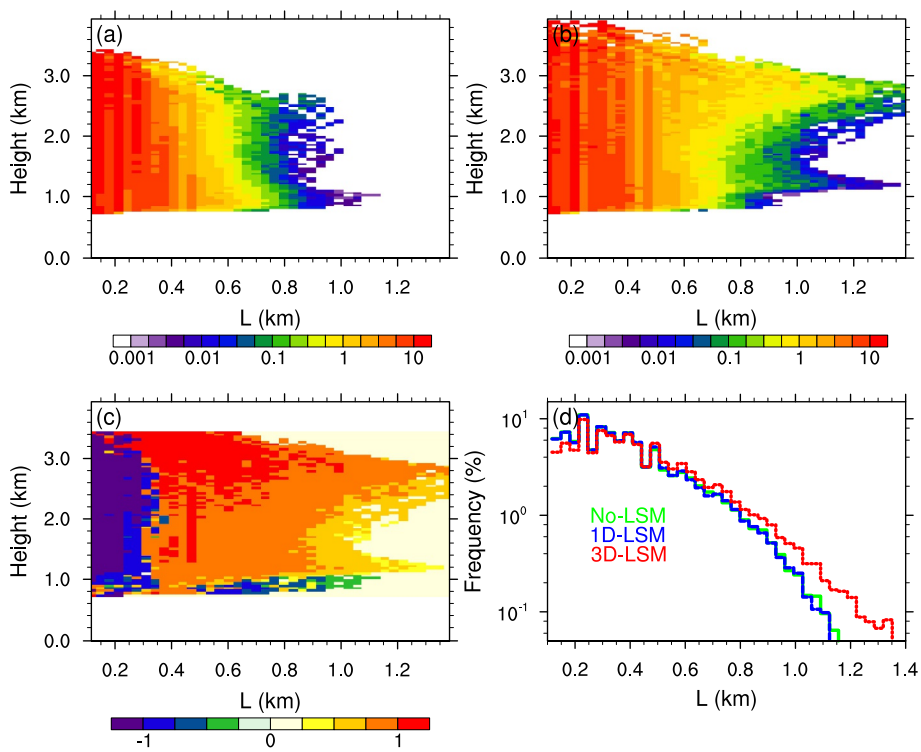


Figure 4. Cloud size distribution for layer clouds at each height in (a) 1D-LSM, (b) 3D-LSM, and (c) their difference. Cloud size distribution for projected clouds is shown in (d). In (d), green, blue, and red curves represent the No-LSM, 1D-LSM, and 3D-LSM experiments, respectively.

19448007, 2026, 14, Downloaded from https://agupubs.onlinelibrary.wiley.com/doi/10.1029/2026GL122790, Wiley Online Library on [17/07/2026]. See the Terms and Conditions (https://onlinelibrary.wiley.com/terms-and-conditions) on Wiley Online Library for rules of use; OA articles are governed by the applicable Creative Commons License

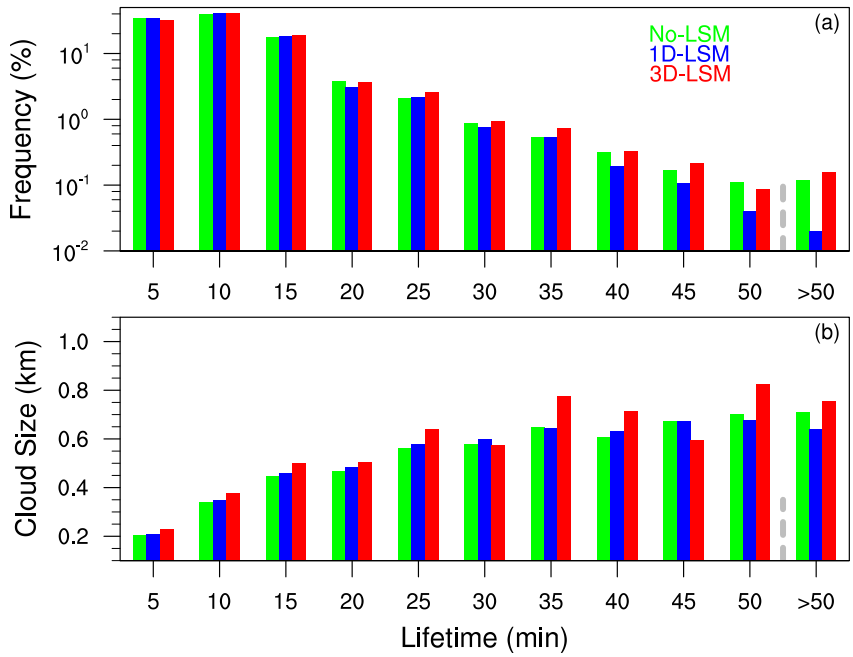


Figure 5. Distribution of cloud lifetime (a) and mean cloud size within each lifetime bin (b). Green, blue, and red bars represent the No-LSM, 1D-LSM, and 3D-LSM experiments, respectively.

distribution tail occurring near 1,100 m in both 1D-LSM and No-LSM. In 3D-LSM, this tail shifts toward larger clouds, reaching approximately 1,400 m. While the distributions between 3D-LSM and 1D-LSM are similar in the 300–600 m bin range, 3D-LSM produces more clouds above this range and fewer below it, indicating that 3D radiative effects promote larger clouds at the expense of smaller ones, a phenomenon reminiscent of cloud aggregation in convective self-organization (Bretherton et al., 2005).

Cloud lifetime is also likely influenced by cloud-shadow-induced surface heterogeneity. Following Dawe and Austin (2012), cloud lifetime is calculated as the length of time that a cloud is tracked. We exclude clouds that end outside the model integration period, as their complete life cycles cannot be determined. The algorithm results in 9,754, 9,967, and 6,790 tracked clouds for the No-LSM, 1D-LSM, and 3D-LSM experiments, respectively. Figure 5a presents the cloud lifetime distribution using a 5-min bin width. In all three experiments, the highest relative frequency occurs for short-lived clouds (lifetime <20 min), and the frequency generally decreases with increasing lifetime. Compared to 1D-LSM, the lifetime distribution shifts toward longer durations in both 3D-LSM and No-LSM, evidenced by an increased proportion of long-lived clouds (lifetime >40 min). Although frequency is plotted in Figure 5a, the cloud number statistics display comparable distributions (Figure S4b in Supporting Information S1). Notably, very few clouds in the 1D-LSM experiment exceed 50 min in lifetime, and the frequency of long-lived clouds (lifetime >50 min) increases from 0.02% in 1D-LSM to 0.12% in No-LSM and 0.16% in 3D-LSM, roughly a sixfold and eightfold increase, respectively. The longer lifetimes and larger sizes of clouds in 3D-LSM point to a coherent relationship between these two cloud properties. Figure 5b plots the mean cloud size within each lifetime bin. As anticipated, shorter-lived clouds tend to be smaller, whereas longer-lived clouds are generally larger. This also explains why No-LSM produces more long-lived clouds: it possesses a relatively higher proportion of larger clouds, consistent with the projected-cloud distribution shown in Figure 4d.

As we can see, although the domain-averaged surface heat fluxes are similar among all three experiments (Figure 2), 3D-LSM exhibits clearly different cloud properties (greater cloud condensate, larger size, longer lifetime) from 1D-LSM and No-LSM. This can be understood as follows. In 1D-LSM, a cold patch (cloud shadow) lies directly beneath a cloud and suppresses its updraft locally, whereas the suppressed cloud is soon replaced by another cloud forming in a neighboring warm patch (clear gap). This negative feedback keeps clouds in 1D-LSM relatively small and short-lived. The spatial compensation between cold and warm patches means that the domain-averaged cloud properties remain nearly unchanged compared to the uniform-flux case (No-LSM); however, cloud size and lifetime tend to be smaller than in No-LSM. In contrast, 3D-LSM produces cold and

19448007, 2026, 14, Downloaded from https://agupubs.onlinelibrary.wiley.com/doi/10.1029/2026GL122790, Wiley Online Library on [17/07/2026]. See the Terms and Conditions (https://onlinelibrary.wiley.com/terms-and-conditions) on Wiley Online Library for rules of use; OA articles are governed by the applicable Creative Commons License

19448007, 2026, 14, Downloaded from https://agupubs.onlinelibrary.wiley.com/doi/10.1029/2026GL122790, Wiley Online Library on [17/07/2026]. See the Terms and Conditions (https://onlinelibrary.wiley.com/terms-and-conditions) on Wiley Online Library for rules of use; OA articles are governed by the applicable Creative Commons License

warm patches through displaced cloud shadows. This configuration favors cloud-scale circulations that actively transport moisture and energy into clouds, leading to positive feedback and thus thicker, larger, and longer-lived clouds.

4. Conclusions

In this study, we use the PALM LES model coupled with the TenStream 3D radiative transfer scheme and an interactive land surface model to investigate the impact of 3D shortwave radiation on cloud condensate, size and lifetime. Three experiments are conducted: 3D-LSM (3D radiation with land-surface coupling), 1D-LSM (1D radiation with land-surface coupling), and No-LSM (no land-surface coupling). Results show 3D-LSM produces higher cloud tops and greater cloud condensate than 1D-LSM, resulting from a substantially larger downward shortwave flux beneath clouds in 3D-LSM. This enhanced radiative flux leads to increased surface temperature, sensible heat flux, and latent heat flux, creating a favorable environment for preexisting clouds by boosting the supply of heat and moisture from the surface, thereby promoting further cloud development. The larger downward shortwave flux beneath clouds in 3D-LSM is primarily attributed to its direct component. There is close similarity between the No-LSM and 1D-LSM experiments regarding domain-mean cloud macrophysical properties.

Using a cloud-tracking algorithm, we find that 3D-LSM produces larger clouds at the expense of smaller ones, shifting the tail of the power-law size distribution from about 1,100 m in 1D-LSM to approximately 1,400 m in 3D-LSM. Regarding cloud lifetime, short-lived clouds dominate in all experiments, but the lifetime distribution shifts toward longer durations in both 3D-LSM and No-LSM compared to 1D-LSM, a shift consistent with the coherent scaling between cloud size and lifetime. Underlying these differences is the contrasting surface heterogeneity induced by each radiation scheme. In 1D-LSM, cloud shadows fall directly beneath clouds, suppressing local updrafts; this negative feedback keeps clouds even smaller and shorter-lived than those in No-LSM. In contrast, 3D-LSM produces cold and warm patches through displaced cloud shadows, which favors cloud-scale circulations that provide positive feedback, leading to thicker, larger, and longer-lived clouds.

Conflict of Interest

The authors declare no conflicts of interest relevant to this study.

Availability Statement

All LES simulation data sets used in this study are available at https://doi.org/10.5281/zenodo.18539571 (Wang & Liu, 2026a). The codes used to analyze the data are available at https://doi.org/10.5281/zenodo.20183219 (Wang & Liu, 2026b).

Acknowledgments

We would like to thank the two anonymous reviewers for their constructive comments that helped to clarify and improve the original paper. This work was jointly supported by the National Key Research and Development Program of China (Grant 2022YFF0802003) and the National Natural Science Foundation of China (Grant 42575163). We acknowledge the National Key Scientific and Technological Infrastructure project "Earth System Science Numerical Simulator Facility" (EarthLab) for providing computational resources.

References

Balsamo, G., Beljaars, A., Scipal, K., Viterbo, P., van den Hurk, B., Hirschi, M., & Betts, A. K. (2009). A revised hydrology for the ECMWF model: Verification from field site to terrestrial water storage and impact in the integrated forecast system. *Journal of Hydrometeorology*, *10*(3), 623–643. https://doi.org/10.1175/2008JHM1068.1

Barker, H. W., Cole, J. N. S., Li, J., Yi, B., & Yang, P. (2015). Estimation of errors in two-stream approximations of the solar radiative transfer equation for cloudy-sky conditions. *Journal of the Atmospheric Sciences*, *72*(1), 4053–4074. https://doi.org/10.1175/JAS-D-15-0033.1

Bony, S., & Dufresne, J.-L. (2005). Marine boundary layer clouds at the heart of tropical cloud feedback uncertainties in climate models. *Geophysical Research Letters*, *32*(20). https://doi.org/10.1029/2005GL023851

Bretherton, C. S., Blossey, P. N., & Khairoutdinov, M. (2005). An energy-balance analysis of deep convective self-aggregation above uniform SST. *Journal of the Atmospheric Sciences*, *62*(12), 4273–4292. https://doi.org/10.1175/JAS3614.1

Brown, A. R., Cederwall, R. T., Chlond, A., Duynkerke, P. G., Golaz, J.-C., Khairoutdinov, M., et al. (2002). Large-eddy simulation of the diurnal cycle of shallow cumulus convection over land. *Quarterly Journal of the Royal Meteorological Society*, *128*(582), 1075–1093. https://doi.org/10.1256/003590002320373210

Cahalan, R. F., Ridgway, W., Wiscombe, W. J., Bell, T. L., & Snider, J. B. (1994). The albedo of fractal stratocumulus clouds. *Journal of the Atmospheric Sciences*, *51*(16), 2434–2455. https://doi.org/10.1175/1520-0469(1994)051<2434:TAOFSC>2.0.CO;2

Chen, J., Hagos, S., Xiao, H., Fast, J. D., & Feng, Z. (2020). Characterization of surface heterogeneity-induced convection using cluster analysis. *Journal of Geophysical Research: Atmospheres*, *125*(20), e2020JD032550. https://doi.org/10.1029/2020jd032550

Cuijpers, J. W. M., & Duynkerke, P. G. (1993). Large eddy simulation of trade wind cumulus clouds. *Journal of the Atmospheric Sciences*, *50*(23), 3894–3908. https://doi.org/10.1175/1520-0469(1993)050<3894:lesotw>2.0.co;2

Dawe, J. T., & Austin, P. H. (2012). Statistical analysis of an LES shallow cumulus cloud ensemble using a cloud tracking algorithm. *Atmospheric Chemistry and Physics*, *12*(2), 1101–1119. https://doi.org/10.5194/acp-12-1101-2012

Deardorff, J. W. (1980). Stratocumulus-capped mixed layers derived from a three-dimensional model. *Boundary-Layer Meteorology*, *18*(4), 495–527. https://doi.org/10.1007/BF00119502

Gristey, J. J., Feingold, G., Glenn, I. B., Schmidt, K. S., & Chen, H. (2020). On the relationship between shallow cumulus cloud field properties and surface solar irradiance. *Geophysical Research Letters*, *47*(22), e2020GL090152. https://doi.org/10.1029/2020GL090152

Gronemeier, T., Kanani-Sühring, F., & Raasch, S. (2017). Do shallow cumulus clouds have the potential to trigger secondary circulations via shading? *Boundary-Layer Meteorology*, *162*(1), 143–169. https://doi.org/10.1007/s10546-016-0180-7

Gu, Y., Liou, K. N., Lee, W. L., & Leung, L. R. (2012). Simulating 3-D radiative transfer effects over the Sierra Nevada Mountains using WRF. *Atmospheric Chemistry and Physics*, *12*(20), 9965–9976. https://doi.org/10.5194/acp-12-9965-2012

Guo, J., Zhang, J., Yang, K., Liao, H., Zhang, S., Huang, K., et al. (2021). Investigation of near-global daytime boundary layer height using high-resolution radiosondes: First results and comparison with ERA5, MERRA-2, JRA-55, and NCEP-2 reanalyses. *Atmospheric Chemistry and Physics*, *21*(22), 17079–17097. https://doi.org/10.5194/acp-21-17079-2021

Hogan, R. J., Schäfer, S. A. K., Klinger, C., Chiu, J. C., & Mayer, B. (2016). Representing 3-D cloud radiation effects in two-stream schemes: 2. Matrix formulation and broadband evaluation. *Journal of Geophysical Research: Atmospheres*, *121*(14), 8583–8599. https://doi.org/10.1002/2016JD024875

Jakub, F., & Mayer, B. (2015). A three-dimensional parallel radiative transfer model for atmospheric heating rates for use in cloud resolving models—The TenStream solver. *Journal of Quantitative Spectroscopy and Radiative Transfer*, *163*, 63–71. https://doi.org/10.1016/j.jqsrt.2015.05.003

Jakub, F., & Mayer, B. (2017). The role of 1-D and 3-D radiative heating in the organization of shallow cumulus convection and the formation of cloud streets. *Atmospheric Chemistry and Physics*, *17*(21), 13317–13327. https://doi.org/10.5194/acp-17-13317-2017

Khairoutdinov, M., & Randall, D. A. (2006). High-resolution simulation of shallow-to-deep convection transition over land. *Journal of the Atmospheric Sciences*, *63*(12), 3421–3436. https://doi.org/10.1175/jas3810.1

Lu, C., Liu, Y., Niu, S., & Vogelmann, A. M. (2012). Observed impacts of vertical velocity on cloud microphysics and implications for aerosol indirect effects. *Geophysical Research Letters*, *39*(21), L21808. https://doi.org/10.1029/2012GL053599

Maronga, B., Banzhaf, S., Burmeister, C., Esch, T., Forkel, R., Fröhlich, D., et al. (2020). Overview of the PALM model system 6.0. *Geoscientific Model Development*, *13*(3), 1335–1372. https://doi.org/10.5194/gmd-13-1335-2020

Maronga, B., & Raasch, S. (2013). Large-eddy simulations of surface heterogeneity effects on the convective boundary layer during the LITFASS-2003 experiment. *Boundary-Layer Meteorology*, *146*(1), 17–44. https://doi.org/10.1007/s10546-012-9748-z

Martin, G. M., Johnson, D. W., & Spice, A. (1994). The measurement and parameterization of effective radius of droplets in warm stratocumulus clouds. *Journal of the Atmospheric Sciences*, *51*(13), 1823–1842. https://doi.org/10.1175/1520-0469(1994)051<1823:tmapoe>2.0.co;2

Mayer, B. (2009). Radiative transfer in the cloudy atmosphere. *EPJ Web of Conferences*, *1*, 75–99. https://doi.org/10.1140/epjconf/e2009-00912-1

Meador, W. E., & Weaver, W. R. (1980). Two-stream approximations to radiative transfer in planetary atmospheres: A unified description of existing methods and a new improvement. *Journal of the Atmospheric Sciences*, *37*(3), 630–643. https://doi.org/10.1175/1520-0469(1980)037<0630:TSATRT>2.0.CO;2

Neggers, R. A. J., Jonker, H. J. J., & Siebesma, A. P. (2003). Size statistics of cumulus cloud populations in large-eddy simulations. *Journal of the Atmospheric Sciences*, *60*(8), 1060–1074. https://doi.org/10.1175/1520-0469(2003)60<1060:SSOCCP>2.0.CO;2

Raasch, S., & Franke, T. (2011). Structure and formation of dust devil–like vortices in the atmospheric boundary layer: A high-resolution numerical study. *Journal of Geophysical Research*, *116*(D16), D16120. https://doi.org/10.1029/2011JD016010

Räisänen, P., Barker, H. W., Khairoutdinov, M. F., Li, J., & Randall, D. A. (2004). Stochastic generation of subgrid-scale cloudy columns for large-scale models. *Quarterly Journal of the Royal Meteorological Society*, *130*(601), 2047–2067. https://doi.org/10.1256/qj.03.99

Ren, Y., Fu, S., & Xue, H. (2023). The sensitivity of a mid-latitude maritime stratocumulus cloud to surface fluxes. *Atmospheric Research*, *293*, 106912. https://doi.org/10.1016/j.atmosres.2023.106912

Saiki, E. M., Moeng, C.-H., & Sullivan, P. P. (2000). Large-eddy simulation of the stably stratified planetary boundary layer. *Boundary-Layer Meteorology*, *95*, 1–30. https://doi.org/10.1023/A:1002428223156

Sherwood, S. C., Webb, M. J., Annan, J. D., Armour, K. C., Forster, P. M., Hargreaves, J. C., et al. (2020). An assessment of earth's climate sensitivity using multiple lines of evidence. *Reviews of Geophysics*, *58*(4), e2019RG000678. https://doi.org/10.1029/2019RG000678

Su, H., Jiang, J. H., Zhai, C., Shen, T. J., Neelin, J. D., Stephens, G. L., & Yung, Y. L. (2014). Weakening and strengthening structures in the Hadley circulation change under global warming and implications for cloud response and climate sensitivity. *Journal of Geophysical Research: Atmospheres*, *119*(10), 5787–5805. https://doi.org/10.1002/2014jd021642

Tijhuis, M., van Stratum, B. J. H., & van Heerwaarden, C. C. (2024). The impact of coupled 3D shortwave radiative transfer on surface radiation and cumulus clouds over land. *Atmospheric Chemistry and Physics*, *24*(18), 10567–10582. https://doi.org/10.5194/acp-24-10567-2024

Tijhuis, M., van Stratum, B. J. H., Veerman, M. A., & van Heerwaarden, C. C. (2023). An efficient parameterization for surface shortwave 3D radiative effects in large-eddy simulations of shallow cumulus clouds. *Journal of Advances in Modeling Earth Systems*, *15*(1), e2022MS003262. https://doi.org/10.1029/2022MS003262

Veerman, M. A., Pedruzo-Bagazgoitia, X., Jakub, F., Vilà-Guerau de Arellano, J., & van Heerwaarden, C. C. (2020). Three-dimensional radiative effects by shallow cumulus clouds on dynamic heterogeneities over a vegetated surface. *Journal of Advances in Modeling Earth Systems*, *12*(7), e2019MS001990. https://doi.org/10.1029/2019MS001990

Wang, K., Dickinson, R. E., & Liang, S. (2008). Observational evidence on the effects of clouds and aerosols on net ecosystem exchange and evapotranspiration. *Geophysical Research Letters*, *35*(10), L10401. https://doi.org/10.1029/2008GL034167

Wang, X. (2017). Effects of cloud condensate vertical alignment on radiative transfer calculations in deep convective regions. *Atmospheric Research*, *186*, 107–115. https://doi.org/10.1016/j.atmosres.2016.11.014

Wang, X., & Liu, Y. (2026a). Parallelized LES model (PALM) outputs of shallow convection with different radiative transfer and land surface coupling configuration. *Zenodo*. [Dataset]. https://doi.org/10.5281/zenodo.18539571

Wang, X., & Liu, Y. (2026b). Visualization scripts for: Parallelized LES model (PALM) outputs of shallow convection with different radiative transfer and land surface coupling configuration. *Zenodo*. [Software]. https://doi.org/10.5281/zenodo.20183219

Wang, X., Miao, H., Liu, Y., & Bao, Q. (2021). Dependence of cloud radiation on cloud overlap, horizontal inhomogeneity, and vertical alignment in stratiform and convective regions. *Atmospheric Research*, *249*, 105358. https://doi.org/10.1016/j.atmosres.2020.105358

Wang, X., & Zhang, M. (2014). Vertical velocity in shallow convection for different plume types. *Journal of Advances in Modeling Earth Systems*, *12*(2), 478–489. https://doi.org/10.1002/2014MS000318

Wapler, K., & Mayer, B. (2008). A fast three-dimensional approximation for the calculation of surface irradiance in large-eddy simulation models. *Journal of Applied Meteorology and Climatology*, *47*(12), 3061–3071. https://doi.org/10.1175/2008JAMC1842.1

Wicker, L. J., & Skamarock, W. C. (2002). Time-splitting methods for elastic models using forward time schemes. *Monthly Weather Review*, *130*(8), 2088–2097. https://doi.org/10.1175/1520-0493(2002)130<2088:TSMFEM>2.0.CO;2

19448007, 2026, 14, Downloaded from https://agupubs.onlinelibrary.wiley.com/doi/10.1029/2026GL122790, Wiley Online Library on [17/07/2026]. See the Terms and Conditions (https://onlinelibrary.wiley.com/terms-and-conditions) on Wiley Online Library for rules of use; OA articles are governed by the applicable Creative Commons License

Williamson, J. H. (1980). Low-storage Runge-Kutta schemes. *Journal of Computational Physics*, *35*(1), 48–56. https://doi.org/10.1016/0021-9991(80)90033-9

Yang, Q., Zhang, F., Zhang, H., Wang, Z., Li, J., Wu, K., et al. (2019). Assessment of two-stream approximations in a climate model. *Journal of Quantitative Spectroscopy and Radiative Transfer*, *225*, 25–34. https://doi.org/10.1016/j.jqsrt.2018.12.016

Zelinka, M. D., Myers, T. A., McCoy, D. T., Po-Chedley, S., Caldwell, P. M., Ceppi, P., et al. (2020). Causes of higher climate sensitivity in CMIP6 models. *Geophysical Research Letters*, *47*(1), e2019GL085782. https://doi.org/10.1029/2019GL085782

Zhang, M. H., & Lin, J. L. (1997). Constrained variational analysis of sounding data based on column-integrated budgets of mass, heat, moisture, and momentum: Approach and application to ARM measurements. *Journal of the Atmospheric Sciences*, *54*(11), 1503–1524. https://doi.org/10.1175/1520-0469(1997)054<1503:CVAOSD>2.0.CO;2

Zhang, Y., Klein, S. A., Fan, J., Chandra, A. S., Kollias, P., Xie, S., & Tang, S. (2017). Large-eddy simulation of shallow cumulus over land: A composite case based on ARM long-term observations at its southern Great Plains site. *Journal of the Atmospheric Sciences*, *74*(10), 3229–3251. https://doi.org/10.1175/JAS-D-16-0317.1

Zhao, Y., Wang, X., Liu, Y., & Wu, G. (2024). Are parameterized entrainment rates as scale-dependent as those estimated from cloud resolving model simulations? *Geophysical Research Letters*, *51*(19), e2024GL110735. https://doi.org/10.1029/2024GL110735

19448007, 2026, 14, Downloaded from https://agupubs.onlinelibrary.wiley.com/doi/10.1029/2026GL122790, Wiley Online Library on [17/07/2026]. See the Terms and Conditions (https://onlinelibrary.wiley.com/terms-and-conditions) on Wiley Online Library for rules of use; OA articles are governed by the applicable Creative Commons License